Materials Today Bio 29 (2024) 101362

Contents lists available at ScienceDirect

Materials Today Bio

journal homepage: www.journals.elsevier.com/materials-today-bio

Killing two birds with one stone: Siglec-15 targeting integrated bioactive glasses hydrogel for treatment of breast cancer bone metastasis

Chengkuan Liu [a,b,1], Yangui Zhong [a,b,1], Haibo Huang [a,b], Siyuan Lan [a,b], Jing Li [e], Deqiu Huang [c,d,**], Wen Zhang [a,b,*]

[a] Research Centre of Basic Integrative Medicine, School of Basic Medical Sciences, Guangzhou University of Chinese Medicine, Guangzhou, Guangdong, 510006, PR China
[b] Department of Medical Biotechnology, School of Basic Medical Sciences, Guangzhou University of Chinese Medicine, Guangzhou, Guangdong, 510006, PR China
[c] School of Medical Information Engineering, Guangzhou University of Chinese Medicine, Guangzhou, Guangdong, 510006, PR China
[d] Intelligent Chinese Medicine Research Institute, Guangzhou University of Chinese Medicine, Guangzhou, Guangdong, 510006, PR China
[e] Second People's Hospital of Shenzhen, Shenzhen, Guangdong, PR China

ARTICLE INFO

Keywords:
Bioactive glass
Siglec-15
Photothermal chemotherapy
Bone metastasis

ABSTRACT

Bone metastasis is a fatal consequence of breast cancer that occurs when patients fail to respond to conventional therapies and mainly result from a vicious cycle involving dysregulated bone homeostasis and uncontrolled tumor growth. Recent research has underscored the significance of Siglec-15, a membrane protein implicated in immunosuppression and osteoclast generation. Targeting Siglec-15 may disrupt the "vicious cycle" that causes bone metastases in patients with breast cancer. Herein, we explored the efficacy of targeting Siglec-15 in conjunction with photothermal chemotherapy to impede the progression of bone metastatic during breast cancer and repair tumor-induced osteolysis. First, we formulated an injectable photothermal bioactive glass (BG)-based hydrogel for the local delivery of Siglec-15 shRNA and doxorubicin. The results demonstrated that the hydrogel could kill tumor cells directly through photothermal chemotherapy, provoke intense immune responses and improve the local immunosuppressive microenvironment, which could effectively prevent tumor metastasis and recurrence in a murine model. The combined effect of BGs and Siglec15 shRNA can normalize dysregulated bone homeostasis at the bone metastasis site and significantly reduced bone destruction. Overall, the use of Siglec-15-targeting integrated BG hydrogels may provide a promising therapeutic strategy for treating bone metastasis caused by breast cancer.

1. Introduction

Breast cancer stands out among all cancers for its high incidence and mortality rates globally, making it the predominant malignant tumor impacting women's lives and health [1]. The majority of deaths associated with breast cancer are attributed to cancer metastasis [2], with bones being the most frequent site for distant metastasis. In fact, the prevalence of bone metastasis in patients with advanced breast cancer can be as high as 75 % [3]. Bone metastasis in breast cancer often induces skeletal-related events, such as osteolytic lesions, bone pain, pathological fracture, spinal cord compression, and hypercalcemia. These complications not only shorten patients' survival but also severely diminish their quality of life [4–6]. Current clinical approaches to managing bone metastases in breast cancer are limited and primarily palliative, encompassing chemotherapy, radiotherapy, and anti-resorptive medications such as bisphosphonates and NF-κB antibody receptor activators [7]. While these treatments can mitigate or postpone skeletal-related events, they do not address the cure of bone metastatic tumors. Moreover, cancer cells are known to disrupt bone homeostasis [8], and antiresorptive drugs have been linked to the development of new metastases in approximately 40 % of patients [9,10]. Recent research indicates that cancer cells do not solely erode bone in the

* Corresponding author. Research Centre of Basic Integrative Medicine, School of Basic Medical Sciences, Guangzhou University of Chinese Medicine, Guangzhou, Guangdong, 510006, PR China.
** Corresponding author. School of Medical Information Engineering, Guangzhou University of Chinese Medicine, Guangzhou, Guangdong, 510006, PR China.
E-mail addresses: huangdeqiu@gzucm.edu.cn (D. Huang), zhangw@gzucm.edu.cn (W. Zhang).
[1] These authors contributed equally to this work.

https://doi.org/10.1016/j.mtbio.2024.101362
Received 11 August 2024; Received in revised form 7 November 2024; Accepted 22 November 2024
Available online 25 November 2024

context of bone metastasis; instead, they engage in a pernicious positive feedback loop with osteoblasts and osteoclasts. This cycle fosters unbridled tumor expansion and intensifies the disruption of bone homeostasis [11,12]. As a result, bone regeneration and tumor growth exist in a delicate balance, posing a significant challenge in the treatment of bone metastasis. Consequently, identifying a target that can inhibit tumor growth while promoting bone regeneration is of paramount importance.

Siglec-15, a member of the salivary acid-binding immunoglobulin-type lectins, is a membrane protein predominantly found in myeloid cells [13]. Emerging research has highlighted Siglec-15 as a pivotal immunosuppressive element within the tumor microenvironment. In this context, cancer cells and tumor-associated macrophages (TAMs) that express Siglec-15 contribute to tumor growth and metastasis by dampening T-cell responses, rendering Siglec-15 a promising target for immunomodulatory cancer therapies [14–16]. Studies have consistently shown that Siglec-15 expression is elevated in various cancers when compared to normal tissues, at both the mRNA and protein levels [15,17]. Moreover, in a melanoma model featuring the B16 cell line overexpressing GM-CSF, the suppression or reduction of Siglec-15 has been shown to enhance T-cell responses and activate tumor-suppressive properties [15]. Additional research has indicated that osteoclasts facilitate the secondary metastasis of breast cancer via Siglec-15, which inhibits the initial activation of $CD8^+$ T-cells [18]. Meanwhile, Siglec-15 also fosters osteoclast differentiation by engaging with DAP12 [19–21], and the inhibition of Siglec-15 abrogates RANKL-induced osteoclastogenesis [22], a process essential for bone resorption. Collectively, these findings suggest that Siglec-15 may be instrumental in bone metastasis and could serve as a dual target for anti-bone resorption and cancer treatments. Consequently, targeting Siglec-15 holds significant promise for the therapeutic management of breast cancer bone metastasis.

Achieving targeted delivery of hairpin RNA (shRNA) to suppress Siglec-15 expression faces numerous challenges, such as limited penetration through tumor tissues, susceptibility to rapid degradation, and the potential for toxicity and adverse side effects in normal tissues [23]. Injectable hydrogels, as drug delivery systems, offer a promising solution by enabling localized shRNA release at the tumor site, thereby mitigating these issues [24]. The localized delivery of shRNA to the tumor lesion can enhance bioavailability and reduce toxicity associated with off-target shRNA absorption by surrounding tissues [25]. Moreover, injectable hydrogels facilitate minimally invasive shRNA administration through syringe injection, owing to their high water content, injectability, customizable properties, and manageable degradation [26,27]. Numerous studies have established FDA-approved sodium alginate (SA) as a non-toxic, highly biocompatible material with broad applications in the food industry and pharmaceuticals [28–31]. In our preliminary research, we developed an SA-based injectable hydrogel delivery system (SA/PEG-CuBGM) for bone tumor treatment [32], demonstrating its efficacy in photothermally eradicating tumors and promoting bone regeneration. However, photothermal therapy alone is not sufficient to prevent tumor recurrence and metastasis, necessitating a combination with immunotherapy. Therefore, integrating Siglec-15 silencing or downregulation with photothermal therapy and chemotherapy, which can induce immunogenic cell death, is more likely to prevent tumor recurrence and metastasis. Previous studies have shown that drug encapsulation and loading capabilities can be enhanced by micronano bioactive glass (BG), which possesses numerous mesoporous structuresand [33–35]. Furthermore, BG's ability to be modified for photothermal functionalization by doping with metal elements makes it an ideal component for combining chemotherapy and photothermal therapyand [36,37]. Also, BG is known to promote osteoblast differentiation and bone formation, which is crucial for bone repair [38,39]. These findings suggest that the combination of BG-based hydrogels with Siglec-15 shRNA holds significant promise for the treatment of bone metastasis in breast cancer, offering a potential therapeutic approach that targets both the tumor and the compromised bone environment simultaneously.

In this study, we have developed a multifunctional injectable BG hydrogel scaffold designed for the targeted delivery of Siglec-15 shRNA to repress its expression. This innovative hydrogel is capable of integrating photothermal chemotherapy, immunotherapy, and bone repair, offering a comprehensive approach to treating bone metastasis in breast cancer. The hydrogel is composed of BG loaded with doxorubicin (DOX) coated with tannic acid/Fe^{3+} deposition, PEI-Siglec-15 shRNA complexes, and SA. As depicted in Scheme 1, after the hydrogel is administered at the tumor site, laser irradiation facilitates rapid in situ gelation and induces a photothermal effect that kills tumor cells, while also triggering immunogenic cell death through the release of doxorubicin. Concurrently, the shRNA targeting Siglec-15 within the bone metastasis niche can alter the ability of Siglec-15 to promote tumor-induced osteoclast formation and inhibit T-cell activity, thereby disrupting the immunosuppressive tumor microenvironment. The dual effects of this treatment aim to not only inhibit the growth of bone metastases but also to normalize bone homeostatic dysregulation.

2. Results

2.1. Fabrication and characterization of the BG-pTA nanoparticles

BG-pTA nanoparticles with an average particle size of 399 nm were prepared by the sol-gel method in combination with the template method (Table S4). SEM imaging revealed that the BG-pTA nanoparticles, when compared to pristine BG, were uniformly coated with a tannic acid/Fe^{3+} complex on their surface, exhibiting excellent dispersion and a distinct spherical morphology (Fig S1 A, B). Consistent with our previous findings that Cu doping does not alter the molecular structure of BG [32], we employed Fourier-transform infrared spectroscopy (FTIR) to analyze the molecular structure of the purified BG-pTA. The results indicated that the primary structure of BG-pTA was characterized by a Si-O network (Fig S1 D). Furthermore, the zeta potential measurements of BG-pTA nanoparticles, along with the elemental mappings of O, Si, Ca, and Fe, substantiated the aforementioned observations (Fig S1 C and Fig S2). To enhance the DOX loading capacity of BG, we optimized the initial DOX concentration and determined that the encapsulation efficiency of BG reached a peak of 96 % at a concentration of 250 g mL^{-1} (Table S5). Consequently, we prepared BG@DOX-pTA nanoparticles with the optimal loading efficiency for subsequent in vitro and in vivo studies.

2.2. Synthesis and characterization of the hydrogel delivery systems

We fabricated an injectable hydrogel delivery system through a dual cross-linking approach, combining the DA click reaction between Fruan-SA and MAL-PEG-MAL, and the ionic cross-linking of Ca^{2+} with SA (Fig. 1A and Table S6). The synthesis of Fruan-SA began with the reaction of furfurylamine with the carboxyl group of SA. Following purification, Fruan-SA was obtained after three days of dialysis, and its molecular structure was confirmed by 1H NMR spectroscopy. The ^1H NMR spectrum exhibited new peaks at 6.3, 6.4, and 7.5 ppm, confirming the successful synthesis of Fruan-SA (Fig. S3A). The resulting pre-gel solution, derived from Fruan-SA, demonstrated excellent injectability, being easily injectable (Fig. 1B). We then documented the gelation times of the hydrogels under various conditions. As shown in Table S7, the presence of BG-pTA significantly reduced the gelation time. FTIR analysis revealed that the absorption peaks of Fruan-SA at 1400 cm^{-1} and 1600 cm^{-1} vanished post-gelation, signifying the completion of the DA click reaction (Fig. 1D).

To simulate the apatite formation ability and degradation of the hydrogels in vivo, the hydrogels were immersed in simulated body fluid (SBF) for 7 days. No obvious apatite formation was observed on the BG-pTA hydrogel surface, while its structure collapsed on day 14 (Fig. S4). The in vitro release kinetic results (Fig. S3B) showed a rapid initial

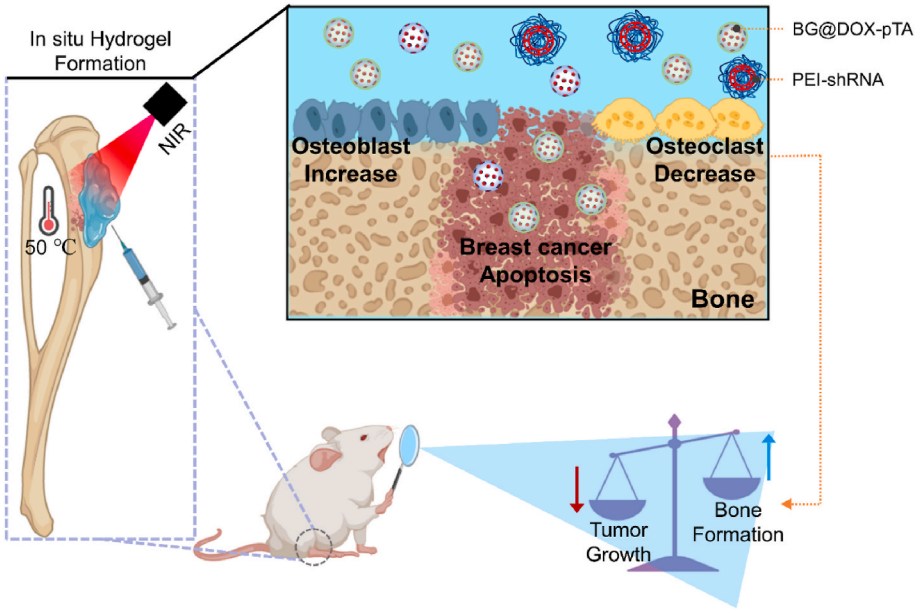

Schema 1. Siglec-15 Targeting Integrated Bioactive Glasses Hydrogel for Treatment of Breast Cancer Bone Metastasis. The hydrogel, composed of a tannic acid/Fe^{3+} coated doxorubicin-loaded BG particles (BG@DOX-pTA), PEI-Siglec-15 shRNA complexes, and sodium alginate (SA), is designed to integrate photothermal chemotherapy, immunotherapy, and bone repair at the tumor site. Upon injection and subsequent laser irradiation, the hydrogel undergoes in situ gelation, generating a localized photothermal-chemotherapy effect that induces immunogenic cell death of cancer cells, while the PEI-shRNA specifically silences Siglec-15, modulating the tumor microenvironment to inhibit osteoclast activity, thereby normalizing bone homeostasis. Ultimately, the dual effects can be achieved to inhibit the tumor growth and normalize bone homeostatic dysregulation in breast cancer bone metastasis.

release of approximately 50 % of the total shRNA within the first 24 h, followed by a sustained release reaching 80 % after 96 h. Notably, this release profile was found to be pH-independent, with no significant differences observed between pH levels of 5.0 and 7.4. The initial burst release of shRNA is attributed to the swelling of the hydrogel, which facilitated the release of the initial dose. Following this initial phase, the hydrogel underwent degradation, leading to a gradual release of the remaining shRNA.

Tissue repair engineered materials must typically exhibit excellent mechanical properties to accommodate the compression of surrounding tissues. SEM images (Fig. 1C) showed that the lyophilized Gel-BG-pTA possessed a more regular and well-defined three-dimensional architecture. In addition, the energy storage modulus G' (Fig. 1E) and compression modulus (Fig. S3C) of the Gel-BG-pTA hydrogel were markedly higher than those of the Gel, significantly greater than those of Gel, except for the loss modulus G'' (Fig. 1F). These findings indicated that the incorporation of BG-pTA nanoparticles significantly improved the mechanical properties of the hydrogels. In rheological assessments, hydrogels exhibited a sol-gel transition at 400 % strain, shear thinning behavior, and self-healing properties, demonstrated by modulus recovery after strain cycles (Fig. S5). These characteristics are pivotal for their injectability and application in tissue engineering and drug delivery systems.

2.3. Photothermal performance of gel-BG-pTA hydrogels

To investigate the photothermal properties of the hydrogels, temperature alterations were monitored by an infrared thermographic camera following near-infrared (NIR) laser irradiation. In a dry setting, the temperature elevation for Gel, Gel-2BG-pTA, Gel-4BG-pTA, and Gel-6BG-pTA hydrogels reached 26.1 °C, 48.7 °C, 53.0 °C, and 54.3 °C, respectively, after a 5-min exposure to NIR radiation at a power density of 1 W cm^{-2} (Fig. 2A–E). Under identical irradiation conditions in PBS, these temperatures rose to 26.3 °C, 47.7 °C, 50.4 °C, and 51.9 °C, respectively (Fig. 2B–F). When the NIR power density was reduced to 0.75 W cm^{-2}, the corresponding temperature increases were 27.0 °C, 47.3 °C, 48.6 °C, and 50.5 °C (Fig. 2C). Moreover, the hydrogels demonstrated consistent photothermal performance across three cycles, indicating their robust photothermal transfer properties (Fig. 2D).

2.4. Bioactive hydrogel materials promoted the proliferation and osteogenic differentiation of MC-3T3-E1 cells

To evaluate the cytocompatibility and bioactivity of the hydrogels on MC-3T3-E1, we cultured MC-3T3-E1 on the surface of hydrogels with and without the incorporation of BG-pTA nanoparticles. After 4 days of incubation, a CCK-8 assay revealed significantly enhanced proliferation in the Gel-2BG-pTA and Gel-4BG-pTA groups compared to the control Gel group (Fig. 3A). This finding was further supported by SEM imaging (Fig. S6A) and F-actin staining (Fig. 3B), which demonstrated not only a higher cell density on the hydrogels in the Gel-2BG-pTA and Gel-4BG-pTA groups but also an increased number of cellular pseudopods, indicating a more active cellular morphology. Conversely, the proliferation of MC-3T3-E1 cells was significantly suppressed in the Gel-6BG-pTA group, attributed to the excessive production of Fe^{3+} ions stemming from an overabundance of BG-pTA nanoparticles. This hypothesis was validated through inductively coupled plasma (ICP) analysis, which quantified the Fe^{3+} concentration in the hydrogel extracts (Fig. S3D). The results underscore the importance of optimizing BG-pTA nanoparticle concentrations to balance bioactivity and cytotoxicity, thereby enhancing the hydrogels' potential for bone tissue engineering applications.

Alkaline phosphatase (ALP) activity is a well-established biomarker for osteoblast activity, detected during both the proliferation and matrix maturation phases of osteoblast development, reflecting the cells' maturity and functionality. To assess the impact of our hydrogel on MC-3T3-E1 osteogenic differentiation, we evaluated ALP activity in MC-3T3-E1 cells following incubation with hydrogel extracts. The Gel-4BG-pTA hydrogel group demonstrated a significant upregulation in ALP expression at 7 and 14 days post-incubation in medium supplemented with the extract (Fig. 3C and D), compared to the control hydrogel group lacking BG-pTA nanoparticles.

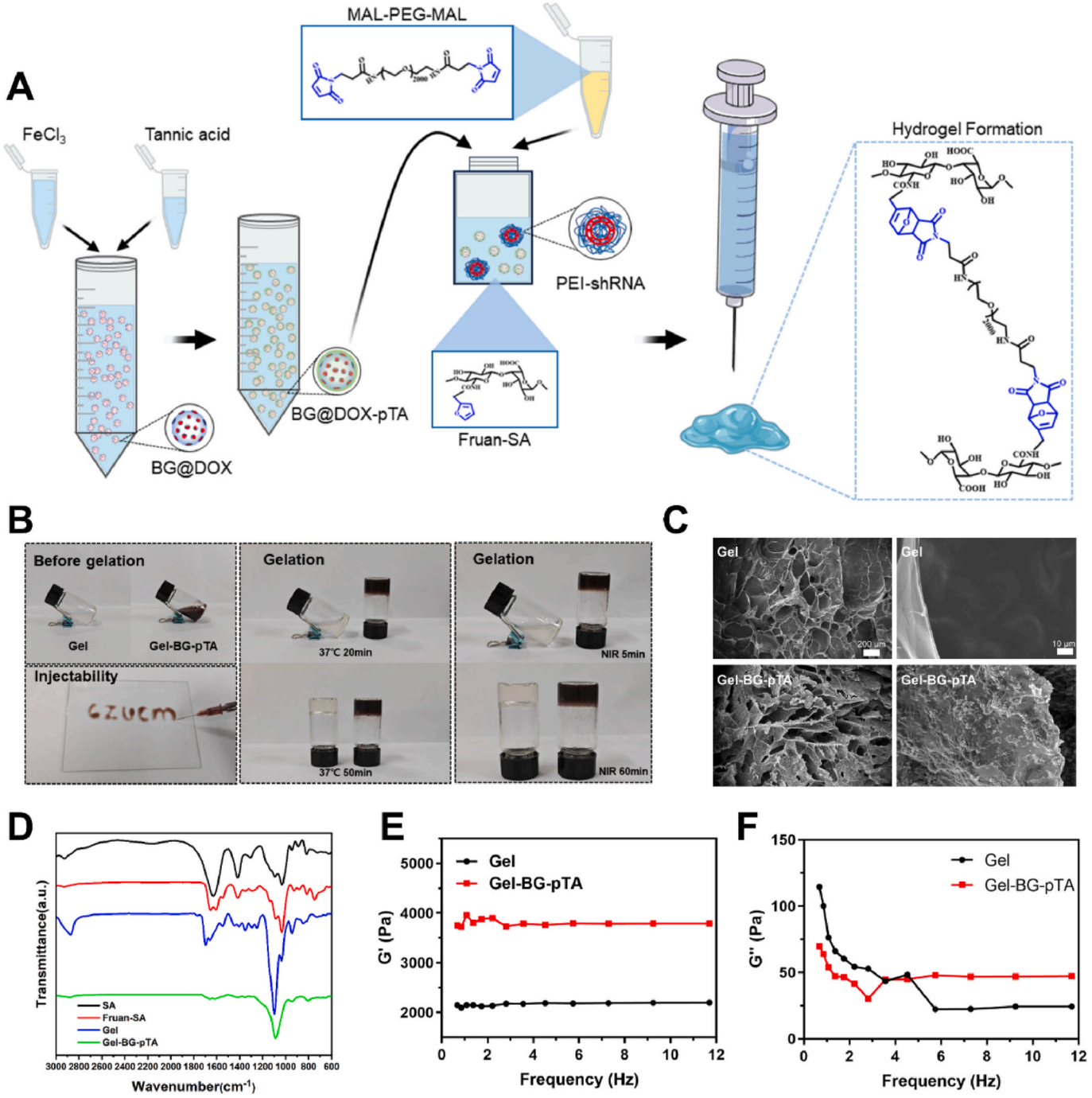

Fig. 1. Preparation and characterization of the Siglec-15 targeting BG hydrogel. (**A**) Schematic illustration of Siglec-15 targeting BG hydrogel formation process. Fruan-SA is subjected to ionic cross-linking with Ca^{2+} ions released from BG@DOX-pTA and click-chemical cross-linking with MAL-PEG-MAL, culminating in the formation of the final hydrogel structure incorporating PEI-shRNA into the hydrogel matrix. (**B**) Images of the injectability and gelation of Gel and Gel-BG-pTA hydrogels under 37 °C or NIR (1.0 W cm^{-2}) irradiation. (**C**) SEM images of Gel and Gel-BG-pTA hydrogels. (**D**) FTIR spectra of injectable hydrogels and their precursors. Rheological assessment of Gel and Gel-BG-pTA hydrogels showing storage modulus G' (**E**) and loss modulus G'' (**F**), respectively.

Incorporation of siglec-15 shRNA into the hydrogel had an insignificant effect on the osteogenic differentiation of MC-3T3-E1 cells (Fig. 3C and D). On day 7, the Gel-4BG-pTA hydrogel notably enhanced the mRNA expression levels of key osteogenic genes RUNX2, COLI, ALP, and OPN in MC-3T3-E1 cells (Fig. 3E). Furthermore, alizarin red staining, used to detect bone-like inorganic calcium deposition, revealed a more intense red color in the Gel-4BG-pTA hydrogel group on day 14 (Fig. S6B), indicating a higher degree of osteogenic differentiation. Collectively, these findings suggest that the Gel-4BG-pTA hydrogel effectively promotes both proliferation and osteogenic differentiation of MC-3T3-E1 cells, highlighting its potential in bone tissue engineering applications.

2.5. *Siglec-15-targeting BG hydrogels inhibit osteoclast formation*

To elucidate the role of Siglec-15 in osteoclast differentiation, we investigated the effect of Siglec-15 shRNA on RANKL-induced osteoclastogenesis in RAW264.7 cells. The efficiency of shRNA transfection in these cells was confirmed by fluorescence imaging and RT-qPCR (Figs. S7 and S8). Morphological analysis revealed that RAW264.7

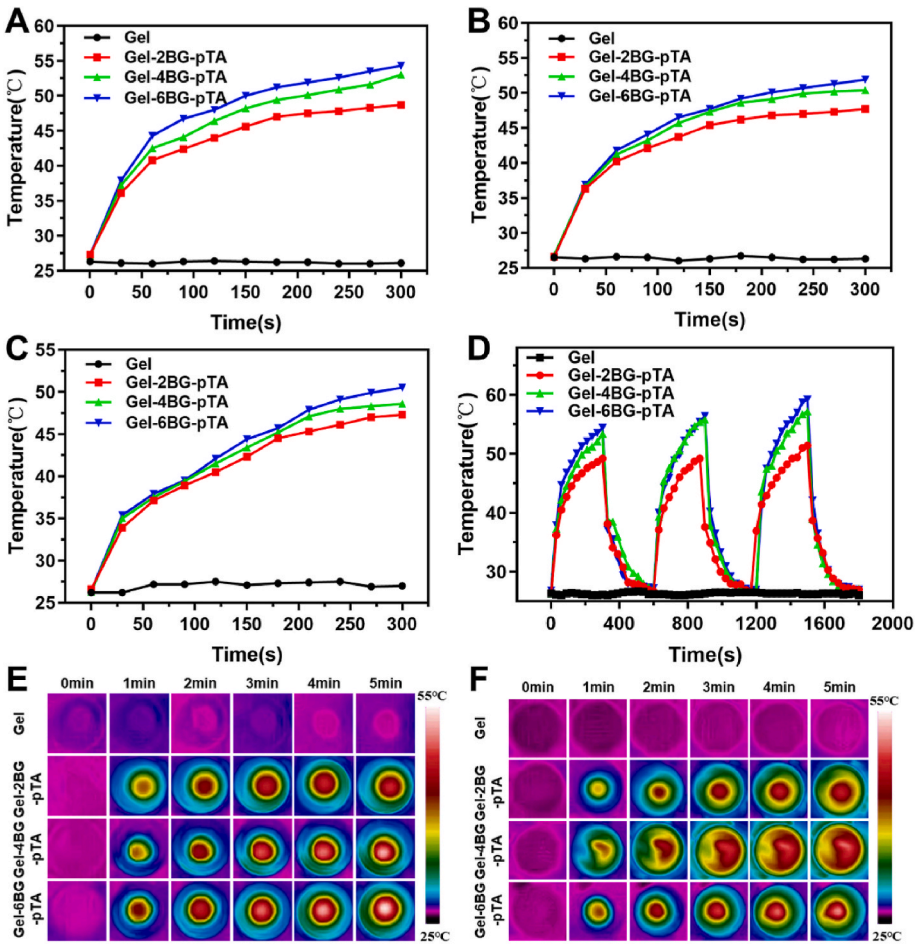

Fig. 2. Photothermal performance of hydrogels with varying incorporation of BG-pTA. Temperature variations of hydrogels exposed to NIR radiation (808 nm, 1.0 W cm^{-2}) for 5 min in dry (**A**) and PBS (**B**) environments, respectively. (**C**) Temperature changes of hydrogels under NIR irradiation (0.75 W cm^{-2}) for 5 min in a dry environment. **(D)** Temperature changes of hydrogels subjected to three cycles of NIR irradiation (1.0 W cm^{-2}) in a dry environment, with each cycle comprising 5 min of laser exposure followed by a 5-min interval without irradiation. Infrared thermal images of hydrogels under 808 nm laser irradiation with a power density of 1.0 W cm^{-2} in n dry (**E**) and PBS (**F**) environments, respectively.

cells differentiated into tartrate-resistant acid phosphatase (TRAP)-positive multinucleated osteoclasts upon RANKL stimulation (Fig. 4A). However, compared to other groups, the Gel-shS15 hydrogel and Gel-4BG-pTA-shS15 hydrogel (abbreviated as Gel-4BT-shS15) groups containing siglec-15 shRNA exhibited significantly suppressed osteoclastic differentiation (Fig. 4A, B and Fig. S9). Furthermore, RT-qPCR results (Fig. 4C) showed that Siglec-15 shRNA released from Gel-shS15 and Gel-4BT-shS15 hydrogels significantly downregulated Siglec-15 expression during osteoclastogenesis following RANKL stimulation. Moreover, the decrease in Siglec-15 expression led to a significantly inhibition to the upregulation of c-Fos, cathepsin K, and TRAP in RNAKL-induced RAW264.7 cells treated with Gel-shS15, Gel-4BT, and Gel-4BT-shS15 (Fig. 4D–F). Notably, the downregulation of Siglec-15 did not decrease the expression level of NFATc1 (Fig. 4G), consistent with the understanding that Siglec-15 absence does not influence the transcriptional regulation of NFATc1 [20]. Theses findings suggest that our prepared Gel-4BT-shS15 hydrogel effectively prevents osteoclast formation, highlighting its potential in modulating bone remodeling processes.

2.6. BG hydrogels targeting Siglec-15 suppressed the growth of breast cancer bone metastases

In vitro studies revealed that hydrogels with 2 % and 4 % incorporation of BG-pTA had no cytotoxicity to 4T1 cells, while 6 % incorporation of BG-pTA obviously decreased the viability of 4T1 cells (Fig. 5A). The Gel+4BDT + NIR group with combined photothermal and chemotherapy resulted in an approximately 70 % reduction in 4T1 cell viability compared to control groups. Notably, the deletion of Siglec-15 did not directly affect 4T1 cell viability, and the Gel-4BG-pTA hydrogel or NIR irradiation alone also displayed no toxicity (Fig. 5B and Fig. S10A). Moreover, it was observed that the addition of DOX in BG-based hydrogels has a significant inhibitory effect on the activity of 4T1 cells and also has a noticeable inhibitory effect on MC-3T3-E1 cells, but its inhibitory effect is relatively smaller compared to the 4T1 group. The addition of DOX has almost no effect on the activity of RAW264.7 cells (Figs. S10B–D). Subsequently, we explored the therapeutic potential of BG hydrogels for the local delivery of Siglec-15 shRNA combined with photothermal chemotherapy in a murine model of breast cancer bone metastasis. The Gel-4BG@DOX-pTA (referred to as Gel-4BDT) and Gel-4BDT-shS15 groups were treated by filling residual tumor site with hydrgels, followed immediately by NIR irradiation for 5 min. The results (Fig. 5C, D and Fig. S11) demonstrated that the temperatures of the tumor sites in both the Gel-4BDT and Gel-4BDT-shS15 groups rose to approximately 50 °C, a threshold known to rapidly induce tumor cell death [40,41]. Tumor volume was recorded every two days for three weeks using a Vernier caliper. Compared to the other groups, Gel-4BDT-shS15 group exhibited the most significant reduction in tumor volume change and notably slowed the rate of tumor growth (Fig. 5E–G). Moreover, Gel-4BDT-shS15 group exhibited a markedly higher survival rate compared to other groups throughout the treatment

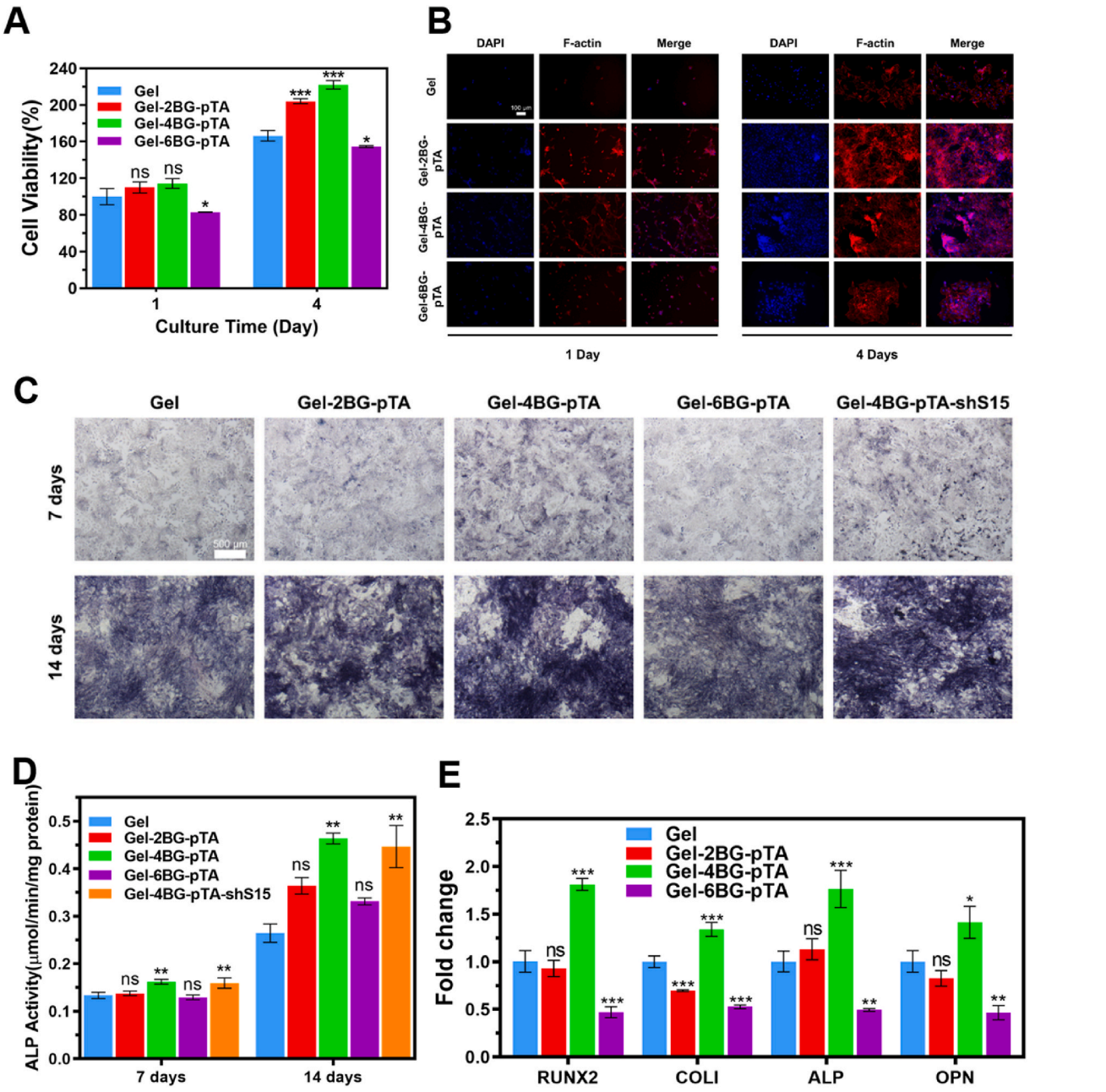

Fig. 3. In vitro assessment of MC-3T3-E1 cell adhesion, proliferation and osteogenic differentiation on hydrogels. (**A**) Proliferation of MC-3T3-E1 cells after 1 day and 4 days co-culturing with hydrogel extracts by CCK-8 assay. (**B**) F-actin staining of MC-3T3-E1 cells on hydrogels after 1 day and 4 days of culture. (**C**) ALP activity staining and (**D**) quantification in MC-3T3-E1 cells after 7 and 14 days of incubation with hydrogel extracts. (**E**) Relative mRNA expression levels of osteogenic markers RUNX2, COLI, ALP, and OPN in MC-3T3-E1 cells, analyzed by RT-qPCR. Data were presented as means ± SD ($n = 3$). Statistical significance was determined using one-way ANOVA. *ns* = not significant, $^{*}p < 0.05$, $^{**}p < 0.01$, $^{***}p < 0.001$ compared to the Gel group.

period (Fig. 5H). After two weeks of treatment, samples of heart, liver, spleen, lung, kidney, tumor and serum were collected from all mice for analysis. Histological examination of tumor tissues using H&E, TUNEL, and Ki67 staining revealed an increased number of apoptotic cells and reduced Ki67 expression in Gel-4BDT-shS15 group (Fig. 5I). Additionally, compared to other groups, Gel-4BDT-shS15 group displayed a decrease in the incidence and size of lung metastases from breast cancer (Fig. 5I and Fig. S12A). Importantly, no significant damage was observed in the H&E staining of major organs (heart, liver, spleen, and kidney) (Fig. S12B), and serum biochemical markers were unremarkable (Fig. S13). These findings suggested that the Gel-4BDT-shS15 hydrogel effectively suppressed the growth and secondary metastasis of breast cancer bone metastases while maintaining good biosafety.

To further investigate the regulatory effects of bioglass (BG)-based hydrogels on the suppressive immune microenvironment in breast cancer bone metastasis, we conducted a flow cytometry analysis to assess the infiltration of immune cells within tumors after treatment with the hydrogel. Immunofluorescence staining (Fig. 6A) showed that locally delivered Siglec-15 shRNA significantly reduced Siglec-15 expression in tumor tissues. Consistent with previous studies that established the potent immunosuppressive role of Siglec-15 in T-cell responses at the tumor site [15], flow cytometry results (Fig. 6B and Fig. S14A) demonstrated a substantial increase in the proportion of $CD8^{+}$ T cells in tumors and spleens following treatment with Gel-4BDT-shS15 hydrogel, compared to PBS group. This suggests that the knockdown of Siglec-15 in tumor tissues, in conjunction with

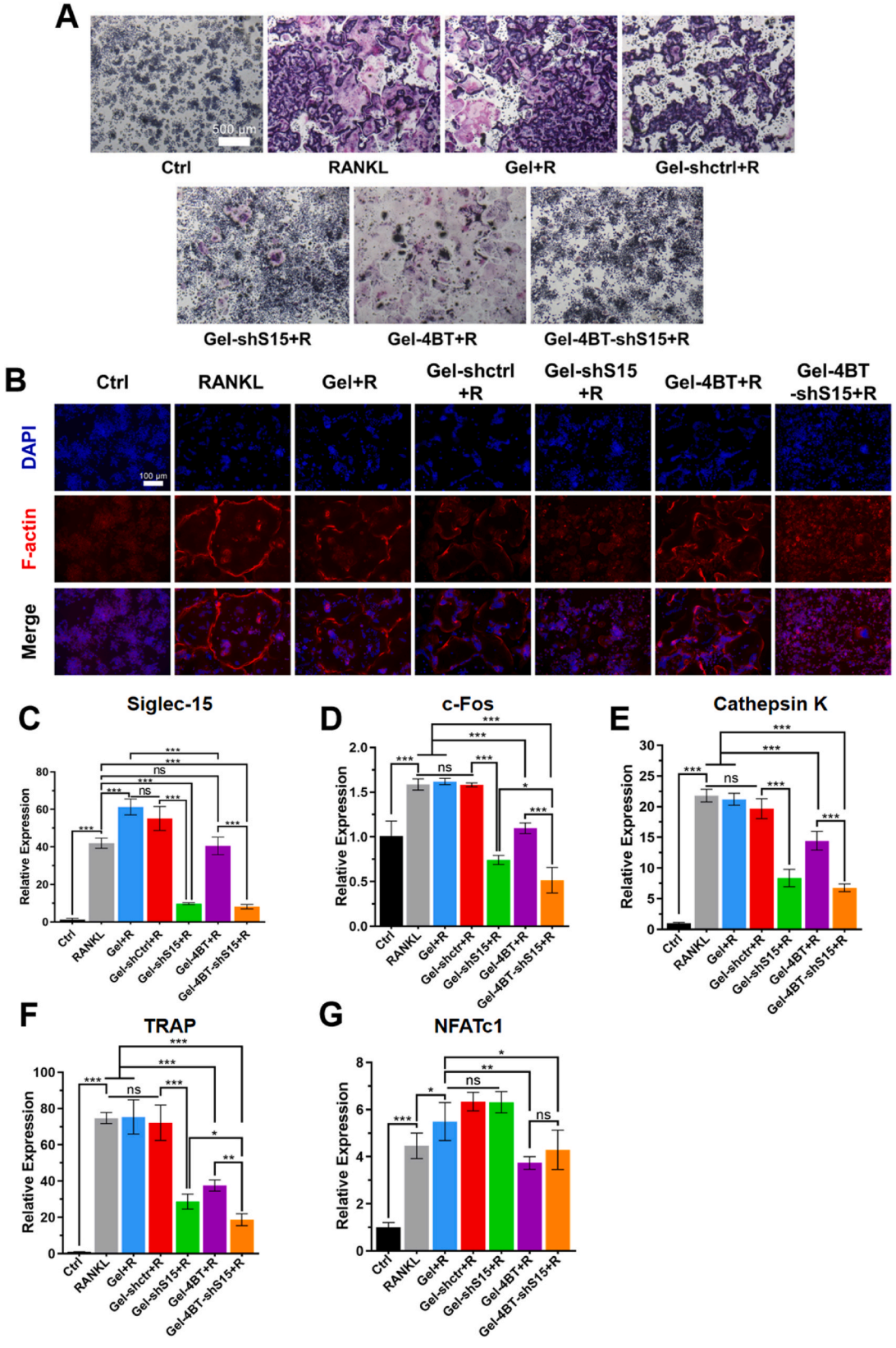

Fig. 4. Siglec-15-targeting BG hydrogels inhibit osteoclast formation in vitro. TRAP (**A**) and F-actin (**B**) staining of RANKL-induced osteoclastogenesis of RAW264.7 cells after 7 days of hydrogel extracts treatment. (**C**) Quantitative analysis of Siglec-15 mRNA expression in RANKL-induced RAW264.7 cells after 7 days of hydrogel extracts treatment. (**D-G**) mRNA expression levels of osteoclastogesis markers c-Fos (**D**), Cathepsin K (**E**), TRAP (**F**) and NFATc1 (**G**) in RANKL-induced RAW264.7 cells after 48 h of hydrogel extracts treatment, as determined by RT−qPCR. Data are presented as means ± SD ($n = 3$). Statistical significance was calculated via one-way ANOVA. *ns* = not significant, $*p < 0.05$, $**p < 0.01$, and $***p < 0.001$.

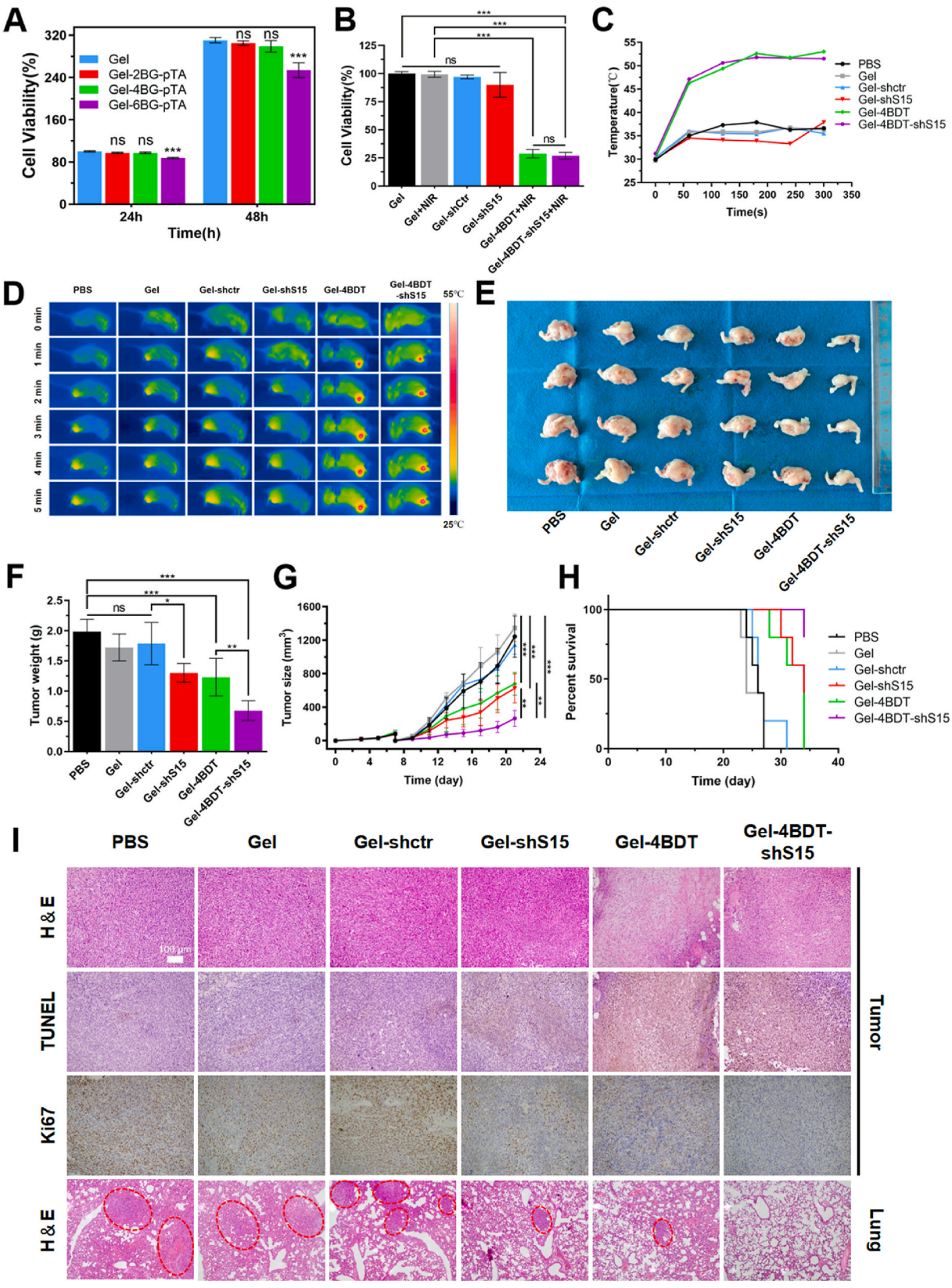

Fig. 5. Inhibiton effect of Siglec-15 targeting BG-based hydrogels on breast cancer bone metastasae. (**A**) CCK-8 results of 4T1 cells cocultured with hydrogels containing varying concentration of BG-pTA for 24 and 48 h. (**B**) Relative viability of 4T1 cells upon NIR (1.0 W cm^{-2}) irradiation for 5 min, following various treatments, as determined by CCK-8 assay. Temperature variation (**C**) and thermal image (**D**) of tumor-bearing mice post NIR (1.0 W cm^{-2}) irradiation for 5 min. (**E**) Photographs of tumor, (**F**) tumor weight, and (**G**) tumor volume changes over 14 days following hydrogel treatment ($n = 5$). (**H**) Kaplan–Meier survival curves of mice across different treatments. (**I**) Histological analysis of tumor tissues via H&E, TUNEL and Ki67 immunohistochemical staining, and H&E staining of lung tissues from mice with bone metastases after 14 days of treatment. The red circle represents metastatic lesions. Data are presented as means ± SD ($n = 3$). Statistical significance was calculated via one-way ANOVA. *ns* = not significant, $*p < 0.05$, $**p < 0.01$ and $***p < 0.001$.

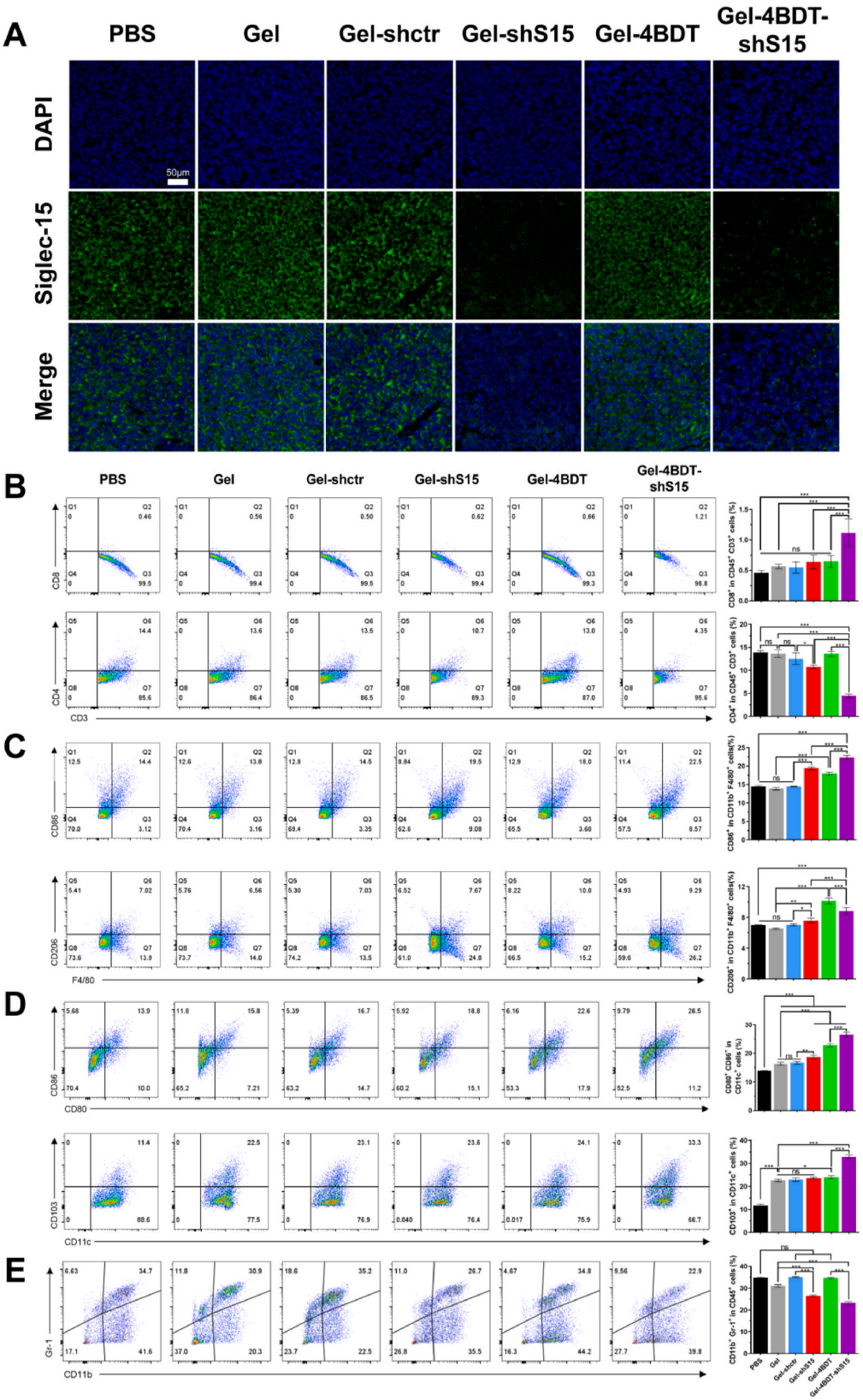

Fig. 6. Siglec-15 targeting BG-based hydrogels promoted an antitumor immune response. (**A**) Immunofluorescence staining of tumor tissues from mice with bone metastasis after 14 days of treatment. (**B**) Representative flow cytometric analysis (left) and relative quantification (right) of T lymphocyte infiltration in tumor tissue gated on $CD45^+CD3^+$ cells. (**C**) Representative flow cytometric analysis (left) and relative quantification (right) of macrophages populations, differentiated as $CD80^+$ M1 and $CD206^+$ M2 phenotypes, gated on $CD45^+CD11b^+F4/80^+$ cells. (**D**) Representative flow cytometric analysis (left) and relative quantification (right) of mature DCs expressing $CD80^+$ $CD86^+$ or $CD103^+$ gated on $CD45^+CD11c^+$ cells. (**E**) Representative flow cytometric analysis (left) and relative quantification (right) of Gr-1^+ MDSCs gating on $CD45^+CD11b^+$ cells. Data are presented as means ± SD ($n = 3$). Statistical significance was calculated via one-way ANOVA. *ns* = not significant, $^*p < 0.05$, $^{**}p < 0.01$, and $^{***}p < 0.001$.

photothermal chemotherapy, could potentiate a robust T-cell response and enhance the cytotoxic effect of T cells on tumor cells. Additionally, compared with PBS group, the frequency of macrophages in tumor tissues was significantly increased after the combined treatment (Fig. 6C), indicating an enhanced phagocytic activity of macrophages against cancer cells. Furthermore, we evaluated the maturation of dendritic cells (DC) in the tumor, which are pivotal for initiating immune response. The results (Fig. 6D) showed that the Gel-4BDT-shS15 group significantly increased the proportion of mature DC expressing CD80, CD86, and CD103, compared to PBS group. Myeloid-derived suppressor cells (MDSC), known for their role in the immunosuppressive microenvironment that promotes tumor growth, recurrence, and metastasis, were significantly reduced from 34.7 % to 22.9 % after treatment with Gel-4BDT-shS15 (Fig. 6E). These findings indicate that BG-based hydrogel targeting Siglec-15, when combined with photothermal chemotherapy, not only stimulates a potent anti-tumor immune response but also alleviates the suppressive immune microenvironment, ultimately leading to a significant inhibition of breast cancer bone metastasis.

2.7. *Siglec-15 targeting BG hydrogel inhibits tumor-induced osteolysis and restores bone homeostasis*

To further evaluate the improvement of tumor-induced osteolysis

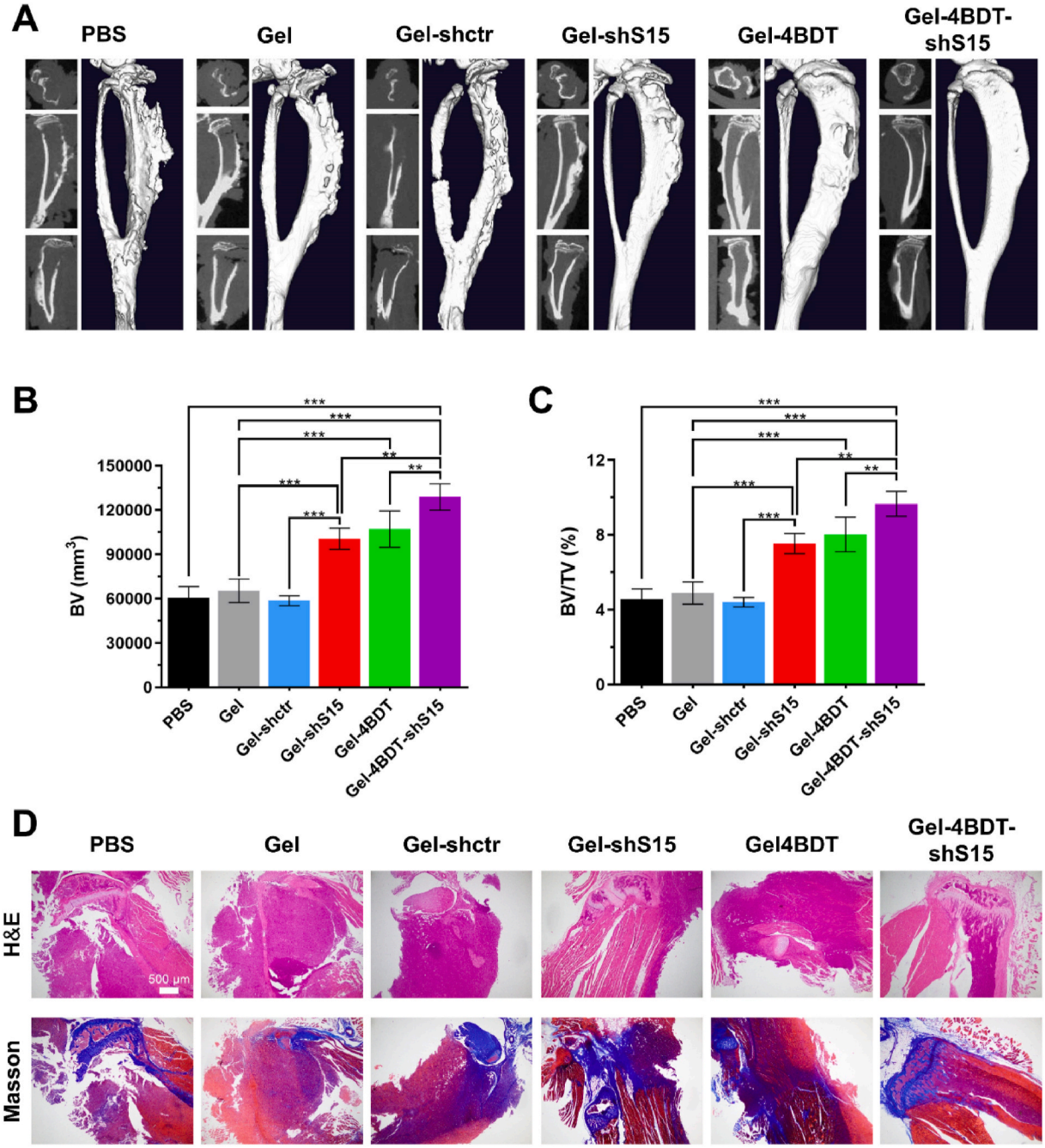

Fig. 7. Siglec-15 targeting BG hydrogel inhibits tumor-induced osteolysis and Restores bone homeostasis. (**A**) Micro-CT images of isolated tibias from mice after a 14-day treatment period. (**B** and **C**) Quantitative analysis of bone volume (BV) and the bone volume/tissue volume ratio (BV/TV). (**D**) Representative H&E and Masson's trichrome staining of tibias from all treatment groups. Data are presented as means ± SD ($n = 3$). Statistical significance was calculated via one-way ANOVA. $^{*}p < 0.01$, $^{***}p < 0.001$.

following treatment of Siglec-15-targeting BG-based hydrogels on breast cancer bone metastasis, osteogenic and osteoclastic differentiation related mRNA expression analysis were firstly conducted to assess the necessity of DOX addition to BG-based hydrogels. The results indicated that DOX addition has a negligible impact on osteogenic differentiation-promoting effect of BG-pTA and its inhibitory effect on osteoclastic differentiation (Fig. S15). Subsequently, right tibiae in each group were harvested from the murine breast cancer bone metastases model after 14 days post-treatment for micro-CT scans. Micro-CT 3D imaging (Fig. 7A) and histological analysis (Fig. 7D) revealed that in the control group (PBS, Gel, Gel-shctr), the tibias of the mice exhibited extensive destruction and substantial tumor cell invasion, indicative of severe tumor-induced osteolysis. In contrast, treatment with Gel-shS15 hydrogel or Gel-4BDT hydrogel resulted in a significant increase in bone volume (BV) and the bone tissue volume ratio (BV/TV) of the tibias (Fig. 7B and C). More notably, treatment with Gel-4BDT-shS15 hydrogel led to a greater BV, preserved marrow cavity integrity, and minimal bone defects (Fig. 7B and C). These results underscore the ability of Siglec-15-targeting BG-based hydrogel to markedly suppress tumor-induced osteolysis, foster bone remodeling, and restore bone homeostatic balance.

3. Discussion

Bone metastasis is the predominant location for the spread of breast cancer, oftern leading to poor. The current clinical prognosis for breast cancer patients with bone metastases remains unsatisfactory, with these patients facing a stark 78 % increased risk of mortality, irrespective of whether they have multiple or single bone metastases [42]. This underscores the pressing need for the development of more effective therapeutic strategies to improve the prognosis for these patients. In addressing breast cancer bone metastasis, a comprehensive approach is imperative-one that not only eradicates cancer cells but also repairs bone defects. Our study introduced an innovative BG-based hydrogel that targets Siglec-15 and integrates photothermal chemotherapy, immunotherapy, and bone repair. This hydrogel system is generated through in situ crosslinking within approximately 5 min, effectively eliminating residual tumors postsurgery while fostering an environment conducive to bone remodeling.

BG is an excellent bone repair material owing to its biocompatibility, ability to bind to bone tissue, and its capacity to stimulate the expression of osteogenic genes [43–45]. The osteogenic potential of BG is attributed to its controlled release of ions such as Ca^{2+} and Si^{4+}, which are integral to bone formation [43–45]. Furthermore, the presence of Fe^{3+} in BG has been shown to enhance osteoblast proliferation and differentiation [46]. In this study, we developed BG-pTA by complexing iron ions with tannic acid to form a complex coating on the surface of BG, endowing it with photothermal properties. Our findings indicated that the incorporation of BG-pTA into the hydrogel enhanced adhension to MC-3T3-E1 cells and significantly promoted their proliferation after 4 days of coculture. Moreover, Gel-4BG-pTA significantly upregulated the expression of RUNX2, COLI, ALP, and OPN in MC-3T3-E1 cells, which was attributed to the activation of osteogenesis-related genes by Ca^{2+}, Fe^{3+}, and Si^{4+} released by BG-pTA. Consistent with previous research, Fe^{3+} concentrations ranging from 0.1 to 1 μg/mL were found to inhibit osteoblast proliferation and differentiationan [47]. Notably, an excessive amount of BG-pTA (Gel-6BG-pTA) resulted in the release of surplus of Fe^{3+} (0.13 μg/mL, Fig. S3D), which in turn suppressed the activity of MC-3T3-E1 cells. Thus, we selected Gel-4BG-pTA for its optimal effect, striking a balance between therapeutic efficacy and cellular compatibility.

Siglec-15, a member of Siglec family, is predominately expressed in myeloid cell populations and plays a pivotal role in immune cell function regulation [13]. In our study, Siglec-15 was found to play a critical role in RANKL-stimulated osteoclast formation and its downregulation could inhibit osteoclast differentiation, which is supported by previous work [19]. Furthermore, the decreased expression of Siglec-15, facilitated by the Gel-shS15 hydrogel, was found to hinder the upregulation of c-Fos, cathepsin K, and TRAP in RANKL-stimulated RAW264.7 cells. Notably, the downregulation of Siglec-15 did not decrease the expression level of NFATc1, as the transcriptional regulation of NFATc1 is independent of Siglec-15, which is consistent with the understanding that different signaling pathways are involved in the regulation of osteoclastogenesis and immune responses [48]. In breast cancer bone metastases, Siglec-15 expression is upregulated in tumor-associated macrophages and cancer cells, leading to suppression of T-cell responses in tumor tissues and promoting bone destruction and bone metastasis [49]. In vitro experiments revealed that downregulation of Siglec-15 had no effect on the activity of 4T1 cells, indicating that its role is more pronounced in the context of the tumor microenvironment and immune cell interactions [48]. In a murine model of osteolytic bone metastasis in breast cancer, downregulation of Siglec-15 effectively inhibited the growth of bone metastases and significantly increased tibia volume after local delivery of shS15. Compared to control group, mice in Gel-shS15 group survived 27–34 days longer, highlighting the therapeutic potential of targeting Siglec-15 in bone metastasis. Nevertheless, the local delivery of shS15 alone was not fufficient to achieve optimal therapeutic effects. When combined with photothermal chemotherapy, the tumor burden and incidence of tumor-induced osteolysis in mice were reduced, and the survival rate was significantly increased.

Furthermore, this combination therapy also significantly promoted T-cell and mature DC activity and altered the suppressive immune microenvironment. Photothermal therapy and chemotherapy have been shown to initiate and promote immunogenic cell death (ICD) in tumors [50–53]. Once tumor cells undergo ICD, they can release tumor-associated antigens that amplify "eat-me" signals, thereby triggering long-term antitumor immune effects [54,55]. Our flow cytometry analysis showed that Gel-4BDT-shS15 significantly increased immune cell infiltration associated with anti-tumor responses, including $CD8^+$ T cells, M1 macrophages, activated DCs, and cDC1. The increased activation of DCs could be attributed to ICD induced by photothermal-chemotherapy [56]. Siglec-15 knockdown further promotes M1 polarization and $CD8^+$ T cell activation. The mechanism by which siglec-15 knockdown promotes M1 polarization of macrophages may be related to cGAS-STING signaling pathway [57]. Siglec-15's role in immunosuppression is noted in bone metastases, and anti-Siglec-15 treatments have shown promise in breast cancer by activating T cells, though the mechanisms are not fully understood. Despite therapeutic success, the molecular mechanisms of anti-Siglec-15 treatment in promoting DC, $CD4^+$, and $CD8^+$ cell activity are poorly understood, with CD44 on osteoclasts and CD11b on T cells suggested as potential ligands [58]. This diversity in Siglec-15 binding underscores the need for further research to clarify its interactions across cell types and validate the underlying biochemical mechanisms. Notably, a relative decrease in $CD4^+$ T cell infiltration in Gel-shS15 and Gel-4BDT-shS15 groups was observed, which might be attributed to an increased proportion of $F4/80^+CD11b^+$ macrophages (Fig. S14B). This suggests that the actual number of $CD4^+$ T cells may not have decreased but was masked by macrophage infiltration. Further analysis showed increased $CD4^+$ T cell infiltration in tumor after 14 days of treatment (Fig. S14C). Additionally, the Gel-4BDT-shS15 group displayed a decrease infiltration of immunosuppressive M2 macrophages and MDSCs, suggesting that combining photothermal chemotherapy with anti-Siglec-15 treatment can improve the immunosuppressive microenvironment and promote an anti-tumor immune response. Overall, Gel-4BDT-shS15 can promote the activation of DCs, increase the infiltration of immune cells that promote tumor immunity, reduce the infiltration of suppressive immune cells, thereby providing assistance to anti-tumor immune responses in eliminating tumors.

Notably, the strengths and differences between our study and other studies in the treatment of bone metastases mainly involve the choice of animal models in the study. Unlike many recent studies that have employed individual subcutaneous tumor models and healthy animal

models of bone defects to investigate the effects of integrated tumor treatment and bone repair on breast cancer bone metastases [59,60], our approach diverges in a significant way. These models fail to accurately simulate the complex interplay between bone tissue destruction and tumor growth driven by vicious cycle of the microenvironment. In contrast, we utilized a direct model, specifically a breast cancer bone metastasis model, to analyze the effects of the integrated hydrogels on metastatic growth and tumor-induced bone imbalance. This method allows for a more realistic simulation of the impact of the "vicious circle" microenvironment on bone homeostasis and metastatic tumor recurrence as seen in actual clinical settings. Moreover, this model enables a more comprehensive assessment of the potential for therapeutic strategies in the treatment of breast cancer bone metastases.

In summary, this study presents the preparation of functionally integrated injectable BG hydrogels targeting Siglec-15, which integrate photothermal chemotherapy, immunotherapy, and bone repair. The potential application of these hydrogels in the treatment of breast cancer bone metastases was evaluated, providing valuable insights for the development of future clinical combination therapies. The functionally integrated BG hydrogel developed for targeting Siglec-15 was found to inhibit the growth of metastases while repairing tumor-induced bone defects. These results suggest that our combination therapy may be beneficial for patients with bone cancer and other cancers with bone metastases, such as lung, prostate, and thyroidthis.

4. Experimental section

Cell culture. The 4T1 cell line and RAW264.7 cell line were purchased from MeilunBio. 4T1 cells were cultured in RPMI-1640 supplemented with 10 % fetal bovine serum (FBS; MeilunBio®, China), 1 % penicillin (100 U mL^{-1}) and 1 % streptomycin (100 μg mL^{-1}) (P/S; Biosharp, China) (Gibco, USA), and RAW264.7 cells were cultured in DMEM (Gibco, USA) supplemented with 10 % FBS (Biosharp, China), 1 % penicillin (100 U mL^{-1}) and 1 % streptomycin (100 μg mL^{-1}). Mouse osteogenic precursor cells (MC-3T3-E1) were purchased from the Cell Bank of the Chinese Academy of Sciences and expanded in α-MEM (Gibco, USA) supplemented with 10 % FBS (Biosharp, China), 1 % penicillin (100 U mL^{-1}) and 1 % streptomycin (100 μg mL^{-1}).

Plasmids. Plasmids were synthesized by Ubigene Biosciences (Guangzhou, China), and the Siglec-15 shRNAs consisted of shRNA1 and shRNA2; the sequence information is shown in Table S1. The Siglec-15 shRNA plasmid in amplified *E. coli* was extracted with a StarPure Endo-free Plasmid Maxi Kit (GenStar, China), and qualified plasmids were screened for subsequent transfection experiments. To verify the transfection efficiency of PEI-shRNA, the PEI-shRNA complex (PEI: shRNA = 2:1) was transfected with RAW264.7 or 4T1 cells preseeded in well plates and observed with a fluorescent cell imager (Bio-Rad, USA).

Synthesis and characterization of BG@DOX-pTA and injectable composite hydrogels. Tannic acid/Fe^{3+} complex-coated DOX-loaded BG (BG@DOX-pTA) was prepared by a sol-gel method combined with a template method. The injectable composite hydrogels were synthesized by chemical cross-linking of DA click between Fruan-SA and MAL-PEG-MAL and ionic cross-linking of Ca^{2+} and SA. All detail preparation and characterization method can be found in the Supporting Information.

Apatite formation capacity and ionic release of hydrogels in vitro. To evaluate the apatite-forming capacity of the hydrogels in vitro, the hydrogels were incubated in SBF, pH 7.4 at 37 °C for 7 days, immersed in deionized water 3 times, and lyophilized, after which the surface of the hydrogels was observed via SEM. To evaluate Ca, Si, P, and Fe ion release from the hydrogels, the sample supernatants were detected by inductively coupled plasma–mass spectrometry (ICP-MS, Agilent, USA) after the hydrogels were immersed in 37 °C PBS for 24 h. To detect shRNA release from hydrogels, sample supernatants were measured at each time point (1, 2, 4, 6, 8, 12, and 24 h) by nucleic acid protein quantification (Nanodrop, Thermo, USA) as described above.

Photothermal properties of the hydrogels. To confirm the photothermal properties of the hydrogels, Gel, Gel-2BG-pTA, Gel-4BG-pTA, and Gel-6BG-pTA hydrogels (diameter: 8 mm, height: 2 mm) were placed in different environments (air, PBS) under irradiation with an 808 nm laser at 0.75 W cm^{-2} and 1.0 W cm^{-2}, and then the temperature variations of the hydrogels were recorded with an infrared thermographic camera (Teledyne FLIR, USA).

Proliferation and osteogenic differentiation of MC-3T3-E1 cells on hydrogels in vitro. To observe the proliferation and adhesion of MC-3T3-E1 cells on the hydrogels, the hydrogels (50 mm^3) were soaked in 75 % ethanol, sterilized for 24 h, washed with PBS, transferred to sterile 24-well plates, and then inoculated with 2×10^4 MC-3T3-E1 cells per well on the hydrogels. After 1 or 4 days of coculture, the removed hydrogels were immersed in 4 % paraformaldehyde for 30 min. The proliferative effect of the hydrogels on the cells was detected by a CCK-8 assay (Hangzhou Fude, China). In addition, to visualize the proliferative and adhesive effects of the hydrogels on MC-3T3-E1 cells, the fixed hydrogels were dehydrated in graded ethanol (50, 70, 80, 90, 95, and 100 % v/v) (60, 30, 20, 5, 5, and 5 min, respectively) and then dried and observed via SEM. Cytoskeletal staining was also performed to evaluate MC-3T3-E1 cell proliferation and adhesion on the hydrogel. Briefly, after 1 or 4 days of coculture, the hydrogels were removed and fixed with 4 % paraformaldehyde, washed with PBS, permeabilized with 0.1 % Triton X-100 for 5 min, and incubated with phalloidin (1:1000 dilution, AAT Bioquest, China) for 1 h in the dark. Then, DAPI (Hubei Servicebio, China) was added for 5 min in the dark, and the staining solution was removed and observed by a fluorescence cell imager (Bio-Rad, USA). To evaluate the effect of hydrogels on MC-3T3-E1 osteoblast formation, alkaline phosphatase (ALP) and alizarin red staining were performed. Briefly, the hydrogels were first soaked in basal medium (20 mg mL^{-1}) at 37 °C on a shaker at 90 rpm for 24 h. The hydrogel extract was obtained by filtering and decontamination at 0.22 μm. MC-3T3-E1 cells were inoculated in 24-well plates at 2×10^4 cells per well, and the hydrogel extract (final concentration of action: 1 mg mL^{-1}) was added and cultured for 7 or 14 days (osteogenic medium: expansion medium + 100 nmol L^{-1} dexamethasone, 50 nmol L^{-1} ascorbic acid, and 10 mmol L^{-1} sodium beta-glycerophosphate) and fixed in 4 % paraformaldehyde for 30 min. This was measured using the BCIP/NBT ALP chromogenic kit (Beyotime, China) and alizarin red kit (Beyotime, China) to stain the cells. We also measured the osteogenic differentiation of MC-3T3-E1 cells by ALP quantification. After 7 or 14 days of incubation, the expression level of ALP was measured using an alkaline phosphatase assay kit (Beyotime, China). To evaluate the effect of the hydrogel on the relative expression levels of MC-3T3-E1 osteogenic genes, MC-3T3-E1 cells were inoculated in 24-well plates at 2×10^4 cells per well and cultured for 7 days with the hydrogel extract (final concentration of action: 1 mg mL^{-1}). Total cellular mRNA was subsequently extracted using the HiPure Total RNA Mini Kit (Magen, China). The RNA was reverse transcribed using a reverse transcription kit (Agbio, China), and the expression levels of ALP, OPN, COL1, and RUNX2 mRNA were detected by RT–qPCR (Bio-Rad, USA); the primer information is listed in Table S2. The mRNA levels were standardized to those of the housekeeping gene GAPDH.

Osteoclastic differentiation of RAW264.7 cells on hydrogels in vitro. To evaluate the ability of the hydrogel delivery system to regulate osteoclastic differentiation in vitro, RAW264.7 cells were inoculated in 24-well plates at 2×10^4 cells/well, stimulated with RANKL (50 ng/mL), cultured for 7 days by adding 50 mm^3 of hydrogel (1.0 μg of shRNA), fixed in 4 % paraformaldehyde for 30 min, and stained using a leukocyte acid phosphatase (TRAP) kit (Sigma–Aldrich, USA). We also measured the osteoclastic differentiation of RAW264.7 cells by cytoskeletal staining. After culturing for 30 min in 4 % paraformaldehyde, the cells were incubated with phalloidin (1:1000 dilution) for 1 h in the dark and then stained with DAPI for 5 min in the dark. The staining solution was removed, and the cells were observed with a fluorescence cell imager. To evaluate the effect of the hydrogel on the relative expression levels of the RAW264.7 osteoclastic differentiation genes, the RAW264.7 cells were

cultured in the presence of the hydrogel upon RANKL induction (50 ng/mL) for 48 h, after which total cellular mRNA was extracted using a HiPure Total RNA Mini Kit. The mRNA was reverse transcribed using a reverse transcription kit, and the expression levels of TRAP, Siglec-15, NFATc1, cathepsin K, and c-Fos mRNA were detected by RT−qPCR; information on the primer is listed in Table S3. The mRNA levels were standardized to those of the housekeeping gene GAPDH.

Development and treatment of the breast cancer bone metastasis murine model. All experimental mice were purchased from Guangzhou Ruige Biotechnology Co. All animal experiments were conducted at the Experimental Animal Center of Guangdong Pharmaceutical University, and the experimental protocols for the mice were approved by the Experimental Animal Committee Inspection of Guangdong Pharmaceutical University. Thirty-six 4-week-old female BALB/c mice were anesthetized with 2 % isoflurane, and each mouse was injected with 1×10^6 4T1 or 4T1-Luc cells near the right anterior tibia. On day 7, all mice were randomly divided into the PBS group, Gel group, Gel-shctrl group, Gel-shS15 (20 μg) group, Gel-4BDT + NIR group (BDT denoted as BG@DOX-pTA), and Gel-4BDT-shS15 + NIR (20 μg) group ($n = 5$), and the tumors were resected, leaving approximately 1 % of the tumor remaining. The residual microtumors were simulated after surgery. Then, the preformed hydrogel (50 μL) was injected into the tumor site. Simultaneously, the Gel-4BT + NIR group and Gel-4BT-shS15 + NIR group were exposed to an 808 nm laser (1.0 W cm^{-2}, 5 min), and the temperature of the tumor was monitored and recorded using an infrared thermography system. Tumor volume was estimated according to the following formula: $width^2 \times length \times 0.5$. Mice were sacrificed on day 21, and tumors, tibiae, and other tissues were collected. Mice were euthanized when the tumor volume reached 2.0 cm^3 or when the body condition was poor.

Bone regeneration analysis. At the end of treatment, the right tibiae of all mice were removed and fixed in 4 % paraformaldehyde solution for 5 days, and the isolated bone tissue was imaged using micro-CT (PerkinElmer, USA). The samples were then decalcified in 10 % EDTA for 3 weeks, dehydrated and embedded in paraffin. All the samples were sectioned (5 μm thickness) using a rotary slicer (CM1860, Leica), and the sections were stained with H&E and Masson's trichrome.

Flow cytometry. The collected mouse tumor tissues were divided into 3–5 mm pieces in precooled PBS, single-cell suspensions were prepared in the presence of collagenase, and the cells were labeled with fluorescent labeling antibodies diluted 200-fold. The fluorescent labeling antibodies used were CD45, CD11b, CD206, F4/80, CD80, Gr-1, CD3, CD4, CD8, CD11c, CD86, and CD103. The stained cells were analyzed using a flow cytometer (BD LSR Fortessa, USA), and the results of the experiments were analyzed using FlowJo software.

Immunohistochemistry and immunofluorescence staining. The tumor tissues were fixed in 4 % paraformaldehyde solution for 5 days, dehydrated and embedded in paraffin. All the samples were sectioned (3.5 μm thick) using a rotary slicer, and the sections were stained with primary and secondary antibodies. The primary antibody used for immunofluorescence staining was rabbit anti-Siglec-15, and the secondary antibody used was FITC-labeled anti-rabbit IgG. Immunofluorescence-stained sections were observed using an inverted fluorescence microscope (Zeiss, Germany). For immunohistochemical staining, the primary antibody used was rabbit anti-Ki67, and the secondary antibody used was HRP-labeled anti-rabbit IgG. Immunohistochemical sections were observed using a light microscope.

Statistical analysis. The results are expressed as the mean ± standard deviation, and one-way analysis of variance (ANOVA) was used for multiple group comparisons. The significance level for all comparisons was $p \leq 0.05$.

CRediT authorship contribution statement

Chengkuan Liu: Writing – original draft, Software, Methodology, Investigation, Formal analysis, Data curation. **Yangui Zhong:** Writing – original draft, Software, Formal analysis, Data curation. **Haibo Huang:** Writing – original draft, Software. **Siyuan Lan:** Formal analysis. **Jing Li:** Formal analysis. **Deqiu Huang:** Writing – review & editing, Funding acquisition. **Wen Zhang:** Writing – review & editing, Funding acquisition, Conceptualization.

Data availability

The data that support the findings of this study are available on request from the corresponding author.

Declaration of competing interest

The authors declare that they have no known competing financial interests or personal relationships that could have appeared to influence the work reported in this paper.

Acknowledgements

This work was supported by the National Natural Science Foundation of China (32000943), the Natural Science Foundation of Guangdong Province (2019A1515010365) and the Basic and Applied Basic Research Foundation of Guangdong Province (2023A1515110788).

Appendix A. Supplementary data

Supplementary data to this article can be found online at https://doi.org/10.1016/j.mtbio.2024.101362.

Data availability

Data will be made available on request.

References

[1] R.L. Siegel, A.N. Giaquinto, A. Jemal, Cancer statistics, 2024, Ca - Cancer J. Clin. 74 (2024) 12–49.
[2] W. Tian, S. Hao, L. Wang, Y. Chen, Z. Li, D. Luo, Pyrotinib treatment enhances the radiosensitivity in HER2-positive brain metastatic breast cancer patients, Anti Cancer Drugs 33 (2022) e622–e627.
[3] R.K. Tahara, T.M. Brewer, R.L. Theriault, N.T. Ueno, Bone metastasis of breast cancer, Adv. Exp. Med. Biol. 1152 (2019) 105–129.
[4] X. Yuan, N. Qian, S. Ling, Y. Li, W. Sun, J. Li, R. Du, G. Zhong, C. Liu, G. Yu, D. Cao, Z. Liu, Y. Wang, Z. Qi, Y. Yao, F. Wang, J. Liu, S. Hao, X. Jin, Y. Zhao, J. Xue, D. Zhao, X. Gao, S. Liang, Y. Li, J. Song, S. Yu, Y. Li, Breast cancer exosomes contribute to pre-metastatic niche formation and promote bone metastasis of tumor cells, Theranostics 11 (2021) 1429–1445.
[5] B. Kim, Y.J. Cho, M. Park, W. Lim, Immunization with RANKL inhibits osteolytic bone metastasis in breast cancer, J. Immunother. 45 (2022) 1–12.
[6] J. Chen, W. Xu, K. Song, L.T. Da, X. Zhang, M. Lin, X. Hong, S. Zhang, F. Guo, Legumain inhibitor prevents breast cancer bone metastasis by attenuating osteoclast differentiation and function, Bone 169 (2023) 116680.
[7] L. Zhang, J. Qu, Y. Qi, Y. Duan, Y.W. Huang, Z. Zhou, P. Li, J. Yao, B. Huang, S. Zhang, D. Yu, EZH2 engages TGFβ signaling to promote breast cancer bone metastasis via integrin β1-FAK activation, Nat. Commun. 13 (2022) 2543.
[8] J. Fornetti, A.L. Welm, S.A. Stewart, Understanding the bone in cancer metastasis, J. Bone Miner. Res. 33 (2018) 2099–2113.
[9] B. Erdogan, I. Cicin, Medical treatment of breast cancer bone metastasis: from bisphosphonates to targeted drugs, Asian Pac J Cancer Prev 15 (2014) 1503–1510.
[10] Adjuvant bisphosphonate treatment in early breast cancer: meta-analyses of individual patient data from randomised trials, Lancet 386 (2015) 1353–1361.
[11] P. Clézardin, Pathophysiology of bone metastases from solid malignancies, Joint Bone Spine 84 (2017) 677–684.
[12] L. Landherr, T. Nagykálnai, [Treatment of bone metastases: bisphosphonates and denosumab], Magy. Onkol. 61 (2017) 175–180.
[13] S. Rashid, D. Song, J. Yuan, B.H. Mullin, J. Xu, Molecular structure, expression, and the emerging role of Siglec-15 in skeletal biology and cancer, J. Cell. Physiol. 237 (2022) 1711–1719.
[14] R. Takamiya, K. Ohtsubo, S. Takamatsu, N. Taniguchi, T. Angata, The interaction between Siglec-15 and tumor-associated sialyl-Tn antigen enhances TGF-β secretion from monocytes/macrophages through the DAP12-Syk pathway, Glycobiology 23 (2013) 178–187.
[15] J. Wang, J. Sun, L.N. Liu, D.B. Flies, X. Nie, M. Toki, J. Zhang, C. Song, M. Zarr, X. Zhou, X. Han, K.A. Archer, T. O'Neill, R.S. Herbst, A.N. Boto, M.F. Sanmamed, S. Langermann, D.L. Rimm, L. Chen, Siglec-15 as an immune suppressor and

potential target for normalization cancer immunotherapy, Nat Med 25 (2019) 656–666.
[16] J. Sun, Q. Lu, M.F. Sanmamed, J. Wang, Siglec-15 as an emerging target for next-generation cancer immunotherapy, Clin. Cancer Res. 27 (2021) 680–688.
[17] S. Shafi, T.N. Aung, V. Xirou, N. Gavrielatou, I.A. Vathiotis, A. Fernandez, M. Moutafi, V. Yaghoobi, R.S. Herbst, L.N. Liu, S. Langermann, D.L. Rimm, Quantitative Assessment of Siglec-15 Expression in Lung, Breast, Head, and Neck Squamous Cell Carcinoma and Bladder Cancer, Laboratory Investigation 102 (2022) 1143–1149.
[18] Y. Wu, H. Ai, Y. Xi, J. Tan, Y. Qu, J. Xu, F. Luo, C. Dou, Osteoclast-derived apoptotic bodies inhibit naive CD8(+) T cell activation via Siglec15, promoting breast cancer secondary metastasis, Cell Rep Med 4 (2023) 101165.
[19] N. Ishida-Kitagawa, K. Tanaka, X. Bao, T. Kimura, T. Miura, Y. Kitaoka, K. Hayashi, M. Sato, M. Maruoka, T. Ogawa, J. Miyoshi, T. Takeya, Siglec-15 protein regulates formation of functional osteoclasts in concert with DNAX-activating protein of 12 kDa (DAP12), J. Biol. Chem. 287 (2012) 17493–17502.
[20] Y. Kameda, M. Takahata, M. Komatsu, S. Mikuni, S. Hatakeyama, T. Shimizu, T. Angata, M. Kinjo, A. Minami, N. Iwasaki, Siglec-15 regulates osteoclast differentiation by modulating RANKL-induced phosphatidylinositol 3-kinase/Akt and Erk pathways in association with signaling Adaptor DAP12, J. Bone Miner. Res. 28 (2013) 2463–2475.
[21] T. Angata, Siglec-15: a potential regulator of osteoporosis, cancer, and infectious diseases, J. Biomed. Sci. 27 (2020) 10.
[22] Y. Wang, Z. Xu, K.L. Wu, L. Yu, C. Wang, H. Ding, Y. Gao, H. Sun, Y.H. Wu, M. Xia, Y. Chen, H. Xiao, Siglec-15/sialic acid axis as a central glyco-immune checkpoint in breast cancer bone metastasis, Proc Natl Acad Sci U S A 121 (2024) e2312929121.
[23] C. Liu, J. Wang, Y. Zhang, W. Zha, H. Zhang, S. Dong, H. Xing, X. Li, Efficient delivery of PKN3 shRNA for the treatment of breast cancer via lipid nanoparticles, Bioorg. Med. Chem. 69 (2022) 116884.
[24] Z. Wang, B. Ding, Y. Zhao, Y. Han, Y. Sheng, L. Tao, X. Shen, J. Zhou, L. Jiang, Y. Ding, Tumor-oriented mathematical models in hydrogel regulation for precise topical administration regimens, J Control Release 345 (2022) 610–624.
[25] L. Zhang, Z. Sun, P. Ren, M. You, J. Zhang, L. Fang, J. Wang, Y. Chen, F. Yan, H. Zheng, M. Xie, Localized delivery of shRNA against PHD2 protects the heart from acute myocardial infarction through ultrasound-targeted cationic microbubble destruction, Theranostics 7 (2017) 51–66.
[26] Y. Li, D. Zhao, Z. Wang, Y. Meng, B. Liu, L. Li, R. Liu, S. Dong, F. Wei, Minimally invasive bone augmentation through subperiosteal injectable hydroxylapatite/laponite/alginate nanocomposite hydrogels, Int. J. Biol. Macromol. 231 (2023) 123232.
[27] X. Xue, Y. Hu, S. Wang, X. Chen, Y. Jiang, J. Su, Fabrication of physical and chemical crosslinked hydrogels for bone tissue engineering, Bioact. Mater. 12 (2022) 327–339.
[28] R. Sharma, R. Malviya, S. Singh, B. Prajapati, A critical review on classified excipient sodium-alginate-based hydrogels: modification, characterization, and application in soft tissue engineering, Gels 9 (2023).
[29] Q. Wei, J. Zhou, Y. An, M. Li, J. Zhang, S. Yang, Modification, 3D printing process and application of sodium alginate based hydrogels in soft tissue engineering: a review, Int. J. Biol. Macromol. 232 (2023) 123450.
[30] A.R. Abbasi, M. Sohail, M.U. Minhas, T. Khaliq, M. Kousar, S. Khan, Z. Hussain, A. Munir, Bioinspired sodium alginate based thermosensitive hydrogel membranes for accelerated wound healing, Int. J. Biol. Macromol. 155 (2020) 751–765.
[31] H. Ning, L. Lu, J. Xu, L. Lu, L. Pan, Z. Lin, Development of sodium alginate-based antioxidant and antibacterial bioactive films added with IRMOF-3/Carvacrol, Carbohydr. Polym. 292 (2022) 119682.
[32] Z. Yang, F. Zhao, W. Zhang, Z. Yang, M. Luo, L. Liu, X. Cao, D. Chen, X. Chen, Degradable photothermal bioactive glass composite hydrogel for the sequential treatment of tumor-related bone defects: from anti-tumor to repairing bone defects, Chem. Eng. J. 419 (2021) 129520.
[33] Y. Zhang, W. Zhang, X. Zhang, Y. Zhou, Erbium-ytterbium containing upconversion mesoporous bioactive glass microspheres for tissue engineering: luminescence monitoring of biomineralization and drug release, Acta Biomater. 168 (2023) 628–636.
[34] M. Schumacher, P. Habibovic, S. van Rijt, Mesoporous bioactive glass composition effects on degradation and bioactivity, Bioact. Mater. 6 (2021) 1921–1931.
[35] S. Gupta, S. Majumdar, S. Krishnamurthy, Bioactive glass: a multifunctional delivery system, J Control Release 335 (2021) 481–497.
[36] Y. Liu, T. Li, H. Ma, D. Zhai, C. Deng, J. Wang, S. Zhuo, J. Chang, C. Wu, 3D-printed scaffolds with bioactive elements-induced photothermal effect for bone tumor therapy, Acta Biomater. 73 (2018) 531–546.
[37] S. Liu, Z. Han, J.N. Hao, D. Zhang, X. Li, Y. Cao, J. Huang, Y. Li, Engineering of a NIR-activable hydrogel-coated mesoporous bioactive glass scaffold with dual-mode parathyroid hormone derivative release property for angiogenesis and bone regeneration, Bioact. Mater. 26 (2023) 1–13.
[38] Z. Xu, X. Qi, M. Bao, T. Zhou, J. Shi, Z. Xu, M. Zhou, A.R. Boccaccini, K. Zheng, X. Jiang, Biomineralization inspired 3D printed bioactive glass nanocomposite scaffolds orchestrate diabetic bone regeneration by remodeling micromilieu, Bioact. Mater. 25 (2023) 239–255.
[39] N. Gómez-Cerezo, L. Casarrubios, M. Saiz-Pardo, L. Ortega, D. de Pablo, I. Díaz-Güemes, B. Fernández-Tomé, S. Enciso, F.M. Sánchez-Margallo, M.T. Portolés, D. Arcos, M. Vallet-Regí, Mesoporous bioactive glass/ε-polycaprolactone scaffolds promote bone regeneration in osteoporotic sheep, Acta Biomater. 90 (2019) 393–402.
[40] Y. Li, K. Zhang, Y. Wu, Y. Yue, K. Cheng, Q. Feng, X. Ma, J. Liang, N. Ma, G. Liu, G. Nie, L. Ren, X. Zhao, Antigen capture and immune modulation by bacterial outer membrane vesicles as in situ vaccine for cancer immunotherapy post-photothermal therapy, Small 18 (2022) e2107461.
[41] X. Li, T. Yong, Z. Wei, N. Bie, X. Zhang, G. Zhan, J. Li, J. Qin, J. Yu, B. Zhang, L. Gan, X. Yang, Reversing insufficient photothermal therapy-induced tumor relapse and metastasis by regulating cancer-associated fibroblasts, Nat. Commun. 13 (2022) 2794.
[42] A. Parkes, C.L. Warneke, K. Clifton, A. Al-Awadhi, O. Oke, R.C. Pestana, O. Alhalabi, J.K. Litton, G.N. Hortobagyi, Prognostic factors in patients with metastatic breast cancer with bone-only metastases, Oncol. 23 (2018) 1282–1288.
[43] M.N. Rahaman, D.E. Day, B.S. Bal, Q. Fu, S.B. Jung, L.F. Bonewald, A.P. Tomsia, Bioactive glass in tissue engineering, Acta Biomater. 7 (2011) 2355–2373.
[44] J.R. Jones, Reprint of: review of bioactive glass: from Hench to hybrids, Acta Biomater. 23 (Suppl) (2015) S53–S82.
[45] E.P. Ferraz, F.S. Oliveira, P.T. de Oliveira, M.C. Crovace, O. Peitl-Filho, M. M. Beloti, A.L. Rosa, Bioactive glass-based surfaces induce differential gene expression profiling of osteoblasts, J. Biomed. Mater. Res. 105 (2017) 419–423.
[46] S. Vahabzadeh, S. Bose, Effects of iron on physical and mechanical properties, and osteoblast cell interaction in β-tricalcium phosphate, Ann. Biomed. Eng. 45 (2016) 819–828.
[47] K. Yamasaki, H. Hagiwara, Excess iron inhibits osteoblast metabolism, Toxicol. Lett. 191 (2009) 211–215.
[48] Matthew S. Macauley, Paul R. Crocker, James C. Paulson, Siglec-mediated Regulation of Immune Cell Function in Disease, 14, 2014, pp. 653–666.
[49] Y. Wang, Z. Xu, K.L. Wu, L. Yu, C. Wang, H. Ding, Y. Gao, H. Sun, Y.H. Wu, M. Xia, Y. Chen, H. Xiao, Siglec-15/sialic Acid axis as a Central Glyco-Immune Checkpoint in Breast Cancer Bone Metastasis, 121, 2024, p. 5.
[50] W. Li, J. Yang, L. Luo, M. Jiang, B. Qin, H. Yin, C. Zhu, X. Yuan, J. Zhang, Z. Luo, Y. Du, Q. Li, Y. Lou, Y. Qiu, J. You, Targeting photodynamic and photothermal therapy to the endoplasmic reticulum enhances immunogenic cancer cell death, Nat. Commun. 10 (2019) 3349.
[51] X. Jiao, L. Sun, W. Zhang, J. Ren, L. Zhang, Y. Cao, Z. Xu, Y. Kang, P. Xue, Engineering oxygen-deficient ZrO(2-x) nanoplatform as therapy-activated "immunogenic cell death (ICD)" inducer to synergize photothermal-augmented sonodynamic tumor elimination in NIR-II biological window, Biomaterials 272 (2021) 120787.
[52] Z. Yu, J. Guo, M. Hu, Y. Gao, L. Huang, Icaritin exacerbates mitophagy and synergizes with doxorubicin to induce immunogenic cell death in hepatocellular carcinoma, ACS Nano 14 (2020) 4816–4828.
[53] Q. Wang, X. Ju, J. Wang, Y. Fan, M. Ren, H. Zhang, Immunogenic cell death in anticancer chemotherapy and its impact on clinical studies, Cancer Lett. 438 (2018) 17–23.
[54] Y. Xi, L. Chen, J. Tang, B. Yu, W. Shen, X. Niu, Amplifying "eat me signal" by immunogenic cell death for potentiating cancer immunotherapy, Immunol. Rev. 321 (2024) 94–114.
[55] Z. Li, X. Lai, S. Fu, L. Ren, H. Cai, H. Zhang, Z. Gu, X. Ma, K. Luo, Immunogenic cell death activates the tumor immune microenvironment to boost the immunotherapy efficiency, Adv. Sci. 9 (2022) e2201734.
[56] M.P. Lenza, L. Egia-Mendikute, A. Antoñana-Vildosola, C.O. Soares, H. Coelho, F. Corzana, A. Bosch, P. Manisha, J.I. Quintana, I. Oyenarte, L. Unione, M. J. Moure, M. Azkargorta, U. Atxabal, K. Sobczak, F. Elortza, J.D. Sutherland, R. Barrio, F. Marcelo, J. Jiménez-Barbero, A. Palazon, J. Ereño-Orbea, Structural insights into Siglec-15 reveal glycosylation dependency for its interaction with T cells through integrin CD11b, Nat. Commun. 14 (2023) 3496.
[57] H. Li, R. Zhu, X. Liu, K. Zhao, D. Hong, Siglec-15 regulates the inflammatory response and polarization of tumor-associated macrophages in pancreatic cancer by inhibiting the cGAS-STING signaling pathway, Oxid. Med. Cell. Longev. 2022 (2022) 3341038.
[58] M.P. Lenza, L. Egia-Mendikute, A. Antoñana-Vildosola, C.O. Soares, H. Coelho, F. Corzana, A. Bosch, P. Manisha, J.I. Quintana, I. Oyenarte, L. Unione, M. J. Moure, M. Azkargorta, U. Atxabal, K. Sobczak, F. Elortza, J.D. Sutherland, R. Barrio, F. Marcelo, J. Jiménez-Barbero, J. Ereño-Orbea, Structural insights into Siglec-15 reveal glycosylation dependency for its interaction with T cells through integrin CD11b, Nat. Commun. 14 (2023) 3496.
[59] Z. Jing, W. Yuan, J. Wang, R. Ni, Y. Qin, Z. Mao, F. Wei, C. Song, Y. Zheng, H. Cai, Z. Liu, Simvastatin/hydrogel-loaded 3D-printed titanium alloy scaffolds suppress osteosarcoma via TF/NOX2-associated ferroptosis while repairing bone defects, Bioact. Mater. 33 (2024) 223–241.
[60] B. Cai, L. Huang, J. Wang, D. Sun, C. Zhu, Y. Huang, S. Li, Z. Guo, L. Liu, G. Feng, Y. Li, L. Zhang, 3D printed multifunctional Ti(6)Al(4)V-based hybrid scaffold for the management of osteosarcoma, Bioconjug Chem 32 (2021) 2184–2194.